Dynamically tunable extraordinary light absorption in monolayer graphene

Alireza Safaei,[1,2] Sayan Chandra,[2] Abraham Vázquez-Guardado,[2,3] Jean Calderon,[4] Daniel Franklin,[1,2] Laurene Tetard,[1,2] Lei Zhai,[2,4] Michael N. Leuenberger,[1,2,3] and Debashis Chanda[1,2,3,*]

[1]*Department of Physics, University of Central Florida, Orlando, Florida 32826, USA*

[2]*NanoScience Technology Center, University of Central Florida, Orlando, Florida 32826, USA*

[3]*CREOL, The College of Optics and Photonics, University of Central Florida, Orlando, Florida 32826, USA*

[4]*Department of Chemistry, University of Central Florida, Orlando, Florida 32805, USA*

(Received 18 May 2017; revised manuscript received 17 August 2017; published 17 October 2017)

The high carrier mobility of graphene makes it an attractive material for electronics, however, graphene's application for optoelectronic systems is limited due to its low optical absorption. We present a cavity-coupled nanopatterned graphene absorber designed to sustain temporal and spatial overlap between localized surface plasmon resonance and cavity modes, thereby resulting in enhanced absorption up to an unprecedented value of theoretically (60%) and experimentally measured (45%) monolayer graphene in the technologically relevant 8–12-μm atmospheric transparent infrared imaging band. We demonstrate a wide electrostatic tunability of the absorption band ($\sim 2\,\mu$m) by modifying the Fermi energy. The proposed device design allows enhanced absorption and dynamic tunability of chemical vapor deposition grown low carrier mobility graphene which provides a significant advantage over previous strategies where absorption enhancement was limited to exfoliated high carrier mobility graphene. We developed an analytical model that incorporates the coupling of the graphene electron and substrate phonons, providing valuable and instructive insights into the modified plasmon-phonon dispersion relation necessary to interpret the experimental observations. Such gate voltage and cavity tunable enhanced absorption in chemical vapor deposited large area monolayer graphene paves the path towards the scalable development of ultrasensitive infrared photodetectors, modulators, and other optoelectronic devices.

DOI: 10.1103/PhysRevB.96.165431

I. INTRODUCTION

Graphene, one of the widely studied two-dimensional materials, possesses a very high carrier mobility and a fast carrier relaxation time [1–5], making it an attractive candidate for ultrafast electronics and optoelectronic devices such as transistors [6], optical switches [7–9], midinfrared (mid-IR) photodetectors [10,11], photovoltaic devices [12], ultrafast lasers [13], etc. The performance of such devices critically depends on the extent of light-matter interaction in graphene, which is limited due to its low optical absorption (<2.5%) in the visible to infrared (IR) wavelength range. Graphene absorption is low across the wide optical wavelength range. In the visible wavelength range, the light absorption in graphene is ~2.3% [14,15], in near-infrared (NIR) it is <2%, in midinfrared (MIR) <3% [15], and in far-infrared range <10% [16]. In nanostructures, light waves propagating at a metal-dielectric interface can excite collective modes of electrons at the metal surface, resulting in the generation of charge density waves called surface plasmons (SPs). There are two types of surface plasmon modes, localized surface plasmons (LSPs) and surface plasmon polaritons (SPPs), propagating along the interface with an effective wavelength much less than that of incident light [17]. Recent studies primarily focused on three approaches to enhance light absorption in monolayer graphene: (i) excitation of surface plasmons on patterned graphene [18–22], (ii) plasmonic light focusing on graphene using metal patterns, as a means to increase absorption of light [7,8,23,24], and (iii) cavity-induced absorption enhancement. In the first category graphene nanoresonator arrays show a mere <12% absorption in the 8–12-μm band [19,21]. In the second category, indirect enhancement methods based on plasmonic effects are employed, where some type of metal pattern is used to enhance the light-graphene interactions [7,8,25–28]. In these approaches the majority of the energy is dissipated as metallic loss [29], which defeats its purpose. In the third category, theoretically, it has been predicted that coupling of patterned graphene with an optical cavity can improve absorption to more than 90% [30,31]. However, the maximum absorption value reported for cavity coupled graphene film was ~30% at $\lambda = 1.5\,\mu$m [21], ~24% absorption in the 5–7-μm wavelength range [22], and less than 20% [32] at $\lambda \sim 8\,\mu$m for isolated graphene nanodisks, which cannot be used for practical applications due to lack of electrical continuity. Enhanced tunable absorption on electrically continuous monolayer graphene is still a scientific challenge.

Here we demonstrate a direct enhancement method based on cavity-coupled patterned monolayer graphene whereby the Fermi energy (E_F) is tuned by an external gate voltage, leading to a predicted maximum absorption of 60% in the 8–12-μm band and a dynamic tunability of up to 2 μm. For the present demonstration we chose the atmospherically transparent 8–12-μm band, since it is essential for infrared thermal imaging and there is a lack of low band-gap absorbers. This 60% absorption can only be achieved if the combined absorption of surrounding layers is <40%. However, the ion gel and the SU-8 polymer films which we used as gate dielectric and cavity spacer layers, respectively, absorb >50% of the amount of the incident light. In order to reduce their absorption to around 45% at $\lambda = 10\,\mu$m, the cavity thickness needs to be decreased to $L = 1.1\,\mu$m. Henceforth, we report the experimentally measured absorption of 45% in the patterned graphene ($A = 1 - R$) with respect to the absorption of the

*debashis.chanda@creol.ucf.edu

structure without graphene as the reference. Remarkably, we achieve a more than 100% improvement in absorption along with a large gate voltage controlled spectral tunability of up to $\sim 2\,\mu$m [22]. This is attributed to the strong coupling between localized surface plasmon resonances (LSPRs) on patterned graphene and the optical cavity modes, the operating band of which is defined by the pattern and cavity dimensions. The surface plasmon couples the incident electromagnetic wave (far field) to the surface wave (near field). This means the amplitude of the excitation field determines the amount of near-field enhancement [17,33–35]. The cavity geometry based on the cavity thickness enhances the excitation field on the patterned graphene due to the constructive interference between the incident field and back reflected field which in turn enhances the LSP on the patterned graphene [17,33–35]. The LSPs in our patterned graphene sheet are edge plasmons that are localized at the edge of each hole [36–38]. The proposed design offers distinct advantages over previous studies. First, this coupled system is more tolerant to the low carrier mobility of CVD graphene, which is evident from the nominal decrease in absorption from 45% for carrier mobility of 960 $\mathrm{cm}^2/\mathrm{V\,s}$ to 31%, as the carrier mobility decreases to 250 $\mathrm{cm}^2/\mathrm{V\,s}$. Second, the feature sizes of nanostructures in this design are much larger than the previous nanoribbon/disk designs [20,32], which reduces fabrication challenges for practical implementation. Finally, the nanoimprinting based large area low cost patterning makes this approach suitable for both enhanced absorption and optoelectronic applications.

II. RESULTS AND DISCUSSION

A. Design and simulation results

An array of nanoholes on graphene conserves the continuity of graphene, and by coupling this perforated graphene to an optical cavity, we show that it is possible to achieve constructive interference between the incident and scattered electric fields, giving rise to strong enhancement of the absorption. Consequently, the strong light-matter interaction amplifies direct light absorption in graphene even in conditions of low carrier mobility, unlike other techniques [18–22] where high carrier mobility is required for absorption enhancement. The system consists of a dielectric slab of thickness L and refractive index $n_d = 1.56$ sandwiched between patterned graphene and an optically thick (200 nm) gold back reflector, as illustrated in Fig. 1(a) right (inset). The patterned graphene is obtained by perforating a square array of holes with 330 nm diameter and 400 nm period. A simple embossing based nanoimprinting technique [35,39] was followed to pattern the graphene sheet. The cavity supports transverse electromagnetic modes when the slab thickness satisfies the phase equation $L = m\lambda/4n_{\mathrm{eff}}$, where n_{eff} is the effective refractive index of the dielectric slab, λ is the incident electromagnetic wavelength, and $m = [1,2,3,\ldots]$ is the mth order of the optical cavity mode. The n_{eff} value, which includes the effect of patterned graphene, is calculated by the effective-medium approach [34,40,41]. The finite-difference time domain (FDTD) simulations (with auto shutoff min of 10^{-8}, simulation time of 5000 fs, and meshing of 0.05 nm) reveal that for odd/even cavity modes excited with x-polarized light, the incident and reflected electric fields interfere constructively/destructively giving

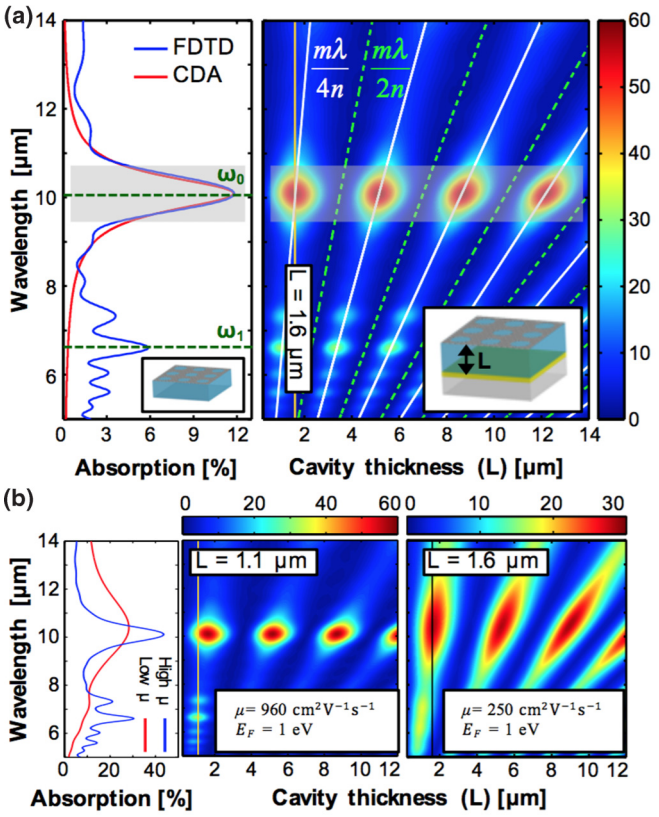

FIG. 1. Extraordinary absorption in cavity-coupled nanomesh graphene and the effect of carrier mobility on absorption enhancement. (a) Left: FDTD and CDA predicted absorption of the patterned graphene. Right: FDTD prediction of absorption as a function of cavity thicknesses for the cavity-coupled case. The white solid and green dotted lines represent constructive and destructive cavity modes respectively. (b) FDTD predicted cavity length and wavelength dependent absorption for high (middle) and low mobility (right). The corresponding wavelength dependent absorption for two cavity thicknesses are shown on left.

rise to a maximum/minimum value in the surface plasmon enhanced absorption for graphene with electron mobility of $\mu = 960\,\mathrm{cm}^2/\mathrm{V\,s}$ and Fermi energy of $E_F = 1.0$ eV [Fig. 1(a) right]. In the case of destructive interference, the incident and reflected electric fields have a phase difference of π such that their interference results in zero net amplitude [17,33,34]. The FDTD absorption spectrum [Fig. 1(a) left] shows two distinct peaks at ω_0 and ω_1, which can be attributed to localized surface plasmon (LSP) and propagating surface plasmon (SPP) modes, respectively. This is evident from the corresponding real [Re(E_z) part and intensity ($|E_z|^2$) of the z component of the electric-field distribution for both plasmonic modes, as shown in Fig. S3a (inset) in the Supplemental Material [42]. The nature of the plasmonic mode at ω_0 is further confirmed to be a LSP because of the close correspondence between the FDTD and coupled dipole approximation (CDA) [41,43] modelled absorption spectra of the patterned graphene without optical cavity [Fig. 1(a) left] [44]. Due to the symmetrical square lattice pattern of the holes, the excitation of LSP is independent of light polarization for normal angle of incidence. The solid white and green dotted

lines in the FDTD calculation in Fig. 1(a) right show the analytical dispersions of the cavity modes as a function of wavelength and cavity thickness, which accurately depicts the origin of this extraordinary absorption arising from the temporal and spatial overlap between the LSP resonance and the cavity modes. The FDTD simulation shows that a cavity length of $L = 1.6\,\mu$m, which satisfies the cavity resonance condition, needs to be chosen in order to achieve ~60% light absorption in patterned graphene at around $\lambda = 10\,\mu$m, giving rise to about a 30-fold absorption enhancement compared to pristine graphene. We use the optical cavity to strongly increase the absorption of the incident light by means of the enhancement of the electric field on the patterned graphene. The bare pattern graphene absorbs ~12% of the incident light [Fig. 1(a)] which is theoretically and experimentally enhanced to ~60% and ~45% for specific cavity lengths at $\lambda = 10\,\mu$m, respectively. A comparison between the uncoupled and the cavity-coupled systems [Figs. 1(a) left and right] shows an increase in absorption from 12% to 60%, without change in the LSP resonance frequency for all cavity modes. The FDTD simulation time was set to 5000 fs, the "auto shut-off time," which defines the convergence as 10^{-8} [this is very small compared to typical simulations for 3D nanostructures (10^{-5})]. The monolayer graphene sheet in FDTD simulation is considered as a bulk material with thickness of 0.5 nm [45,46]. This means the simulation always completely converges. Moreover, the periodic boundary condition ensures better convergence. To show the effect of auto shut-off time on the results, the absorption of patterned graphene for different auto shut-off times are overlaid in Fig. S1 in the Supplemental Material [42]. For all these plots the ripples are present, which means that the ripples are not artifacts of the FDTD simulation. The simulation for shorter time steps and the results were the same. These ripples are the different modes emerging at lower wavelengths because of the diffraction of surface electromagnetic (em) waves. There is no diffraction for the incident light because the period of the pattern is less than the wavelength of the incident light. But, the wavelength of the propagating surface wave is much less than that of free space, resulting in diffractions that are seen as ripples. For graphene in an asymmetric dielectric medium, the plasmon wave number (k_p) can be calculated by means of

$$\frac{\varepsilon_1}{q_{z1}} + \frac{\varepsilon_2}{q_{z2}} + 2\sigma^{\text{intra}}(\omega) = 0, \tag{1}$$

where ε_1 and ε_2 are dielectric functions of adjacent environments, $q_{z1,2} = \sqrt{\varepsilon_{1,2} - (k_p/k)^2}$ and k is the wave number of incident em wave [47,48]. The plasmon diffraction orders correspond to the solutions of Eq. (1) [49], which leads to different peaks at lower wavelengths.

For analytical calculation of the optical extinction of the perforated graphene in the long-wavelength limit, each element is considered as an electric dipole in the electrostatic limit with a specific polarizability $\alpha(\omega)$. The polarizability of a generalized ellipsoidal nanoparticle is [43,50]

$$\alpha(\omega) = \varepsilon_0 V \frac{\varepsilon - \varepsilon_m}{\varepsilon + L_e(\varepsilon - \varepsilon_m)}, \tag{2}$$

where ε and ε_m are the dielectric functions of the conductive element and surrounding medium, respectively. V defines the volume, and the shape factor of the ellipsoid, L_e, is given by

$$L_e = \frac{abc}{2}\int_0^\infty \frac{dq}{(a^2+q)\{(q+a^2)(q+b^2)(q+c^2)\}^{1/2}}, \tag{3}$$

where a is the diameter of the ellipsoid along the light polarization direction, b and c are the diameters along the other two dimensions. For the graphene disk array, $a = b = d$, where d is the disk diameter and $c = t$, where t is the thickness of graphene. To calculate the light absorption of perforated graphene, the light reflection/transmission of graphene disk array is used as light transmission/reflection of graphene hole array. This is an approximation to calculate the optical responsivity of perforated metal by the coupled-dipole approximation (CDA) approach. Derivation of the LSP frequency is possible by calculation of the total electric potential in presence of two-dimensional nanostructure elements. The total electric potential in space is due to the combination of the radiation of the graphene nanostructure and the external electric field, i.e.,

$$\phi(\mathbf{r}) = \phi^{\text{ext}}(\mathbf{r}) - \frac{i}{\omega}\int_0^d\int_0^{2\pi} \frac{d^2\mathbf{r}'\nabla'\cdot\sigma(\mathbf{r}',\omega)\nabla'\phi(r')}{|\mathbf{r}-\mathbf{r}'|}. \tag{4}$$

By considering homogeneous doping of graphene, it can be assumed that the conductivity does not depend on position, and outside graphene the conductivity goes to zero. It means that $\sigma(\mathbf{r},\omega) = \Gamma(\mathbf{r})\sigma(\omega)$, where $\Gamma(\mathbf{r}) = 1/0$ for inside/outside graphene. By defining a dimensionless variable $\mathfrak{R} = \frac{\mathbf{r}}{d}$, the electric potential is given by

$$\phi(\mathbf{r}) = \phi^{\text{ext}}(\mathbf{r}) + \mathfrak{Y}\int_0^1\int_0^{2\pi} \frac{d^2\mathfrak{R}'\nabla'.\,\Gamma(\mathfrak{R}')\,\nabla'\phi(\mathfrak{R}')}{|\mathfrak{R}-\mathfrak{R}'|}, \tag{5}$$

where

$$\mathfrak{Y} = \frac{e^2 E_F}{\pi\hbar^2\varepsilon_m d}\frac{1}{\omega(\omega + i\tau^{-1})}. \tag{6}$$

Equation (5) introduces a self-consistent potential that in the absence of external potential has real eigenvalues related to the plasmonic modes. The LSP frequency is given by [20]

$$\omega_p = \frac{e}{\hbar}\sqrt{\frac{\mathfrak{T}E_F}{\pi\varepsilon_m d}} - \frac{i}{2\tau}, \tag{7}$$

where $\mathfrak{T}$ is the eigenvalue of Eq. (5) and can be derived by solving this eigensystem or by using the results from the FDTD simulation. The imaginary part of ω_p is responsible for the bandwidth of the absorption peak. In addition, Eq. (7) can be applied for the graphene nanoribbon by replacing d (diameter) with w (nanoribbon width) [46].

The lattice contribution S describes the near-field and far-field coupling of the electric dipoles [51],

$$S = \sum_{j\neq i}\left[\frac{(1-ikr_{ij})(3\cos^2\theta_{ij}-1)e^{ikr_{ij}}}{r_{ij}^3} + \frac{k^2\sin^2\theta_{ij}e^{ikr_{ij}}}{r_{ij}}\right], \tag{8}$$

where r_{ij} is the distance between electric dipoles i and j, θ_{ij} is the angle between dipole j, and $\overrightarrow{r_{ij}}$, and $k = \omega/c$ defines the wave number.

The optical reflection coefficient of the disk array can be calculated by using the polarizability and the lattice contribution [43],

$$r_{\text{disk}} = \frac{\pm i\mathfrak{G}}{\alpha^{-1} - S}, \tag{9}$$

where

$$\mathfrak{G}\frac{2\pi k}{A}\begin{cases}(\cos\vartheta)^{-1}, & s-\text{polarization}\\ \cos\vartheta, & p-\text{polarization}\end{cases}, \tag{10}$$

and ϑ is the incident angle, which is zero in our study, A is the area of the unit cell, and positive/negative sign stands for s/p polarization. The transmission coefficient of the disk array can be obtained through $t_{\text{disk}} = 1 + r_{\text{disk}}$.

The absorption enhancement further depends on the electron mobility [52] and Fermi energy of graphene [19,22,28,53,54], which in turn is affected by the choice of dielectric material, substrate, and gate bias. It is well known that graphene on a polymer substrate has a low carrier mobility [5,55] ($< 1000\,\text{cm}^2/\text{V s}$) because of extra scattering processes. Typical scattering centers consist of charge impurities, polymers residues, and coupling centers between graphene electrons and polar or nonpolar optical phonons of the polymer matrix [52,56,57]. To study the impact of the reduced carrier mobility of patterned graphene on its absorption spectra, we performed FDTD simulations for two different carrier mobilities (μ) of $960\,\text{cm}^2/\text{V s}$ and $250\,\text{cm}^2/\text{V s}$. while maintaining the same E_F for the cavity-coupled system. In the FDTD simulations, the real and imaginary parts of graphene's refractive index (n,k) were calculated from the carrier mobility using the random-phase approximation (RPA). In RPA, for high frequencies the complex graphene conductivity is given by [2–4]

$$\sigma(\omega) = \frac{e^2\omega}{i\pi\hbar^2}\left[\int_{-\infty}^{+\infty} d\varepsilon \frac{|\varepsilon|}{\omega(\omega + i\tau^{-1})}\frac{d\rho_F(\varepsilon)}{d\varepsilon} - \int_{-\infty}^{+\infty} d\varepsilon \frac{\rho_F(-\varepsilon) - \rho_F(\varepsilon)}{(\omega + i\delta)^2 - 4\varepsilon^2}\right], \tag{11}$$

where $\delta \to 0$ is the infinitesimal parameter that is used to bypass the poles of the integral. The first and second terms correspond to the intraband electron-photon scattering processes and direct electron interband transitions, respectively. By performing the first integral, the intraband scattering is found to be similar to the Drude conductivity at low temperature $k_BT \ll E_F$ [3],

$$\sigma^{\text{intra}}(\omega) \approx i\frac{e^2E_F}{\pi\hbar^2(\omega + i\tau^{-1})}, \tag{12}$$

where k_B is the Boltzmann constant and T is the temperature. At high em wave frequencies in the visible domain $\hbar\omega \gg (E_F, k_BT)$ where E_F is the Fermi energy with respect to the charge neutrality point (CNP) of the Dirac cone, interband transitions dominate and the light absorbance of graphene is $A = \pi\alpha \approx 2.3\%$, which is independent of wavelength ($\alpha \approx 1/137$ is the fine structure constant) [4]. However, in the mid-IR frequency range and for high Fermi energy $E_F \gg \hbar\omega$, graphene's optical response is dominated by intraband transitions and the conductivity (σ) follows the Drude-Lorentz model [2–4], i.e., Eq. (12), where τ is the relaxation time determined by impurity scattering (τ_{imp}) and electron-phonon ($\tau_{\text{el-ph}}$) interaction time as $\tau^{-1} = \tau_{\text{imp}}^{-1} + \tau_{\text{el-ph}}^{-1}$ [54]. According to the charge conservation law, the relation of the bulk current J_V and the surface current J_S for a material is given by [58]

$$\iint \boldsymbol{J}_S d\boldsymbol{s} = \iiint J_V dV, \tag{13}$$

which means the relation of two- and three-dimensional conductivity is defined by

$$\sigma_{3D} = \frac{\sigma_{2D}}{t}, \tag{14}$$

where t describes the thickness of the material. The dielectric function of graphene can be obtained via its ac conductivity by means of [59]

$$\varepsilon(\omega) = \varepsilon_g + \frac{i\sigma_{3D}}{\varepsilon_0\omega}, \tag{15}$$

where $\varepsilon_g = 2.5$ is the dielectric constant of graphite. Substituting Eq. (14) into Eq. (15) gives the in-plane dielectric function of graphene, i.e.,

$$\varepsilon(\omega) = \varepsilon_g + \frac{i\sigma^{\text{intra}}}{\varepsilon_0\omega t} = \varepsilon_g - \frac{e^2E_F}{\pi\hbar^2\varepsilon_0\omega(\omega + i\tau^{-1})t}, \tag{16}$$

whereas the surface-normal component is $\varepsilon_z = 2.5$. The $\varepsilon(\omega)$ values calculated using Eq. (16) were used to obtain the (n,k) values for the FDTD simulations performed for different Fermi energies.

Figure 1(b) left shows a nominal decrease in the peak absorption from 45% to 31% as the electron mobility is decreased. For a relatively high carrier mobility ($960\,\text{cm}^2/\text{V s}$) loss is small and therefore the bandwidth of the absorption spectrum is narrow, indicating an increased lifetime of plasmons, as observed in Figs. 1(b) middle and 1(b) left (blue) for a cavity thickness of $L = 1.1\,\mu\text{m}$ (this cavity thickness is chosen to show nearby high frequency weaker resonances). Higher loss in lower carrier mobility graphene gives rise to reduced plasmon lifetime and broadening of absorption spectrum, as shown in Figs. 1(b) right and 1(b) left (red). The results from the FDTD simulations demonstrate that our device architecture can induce considerable absorption for low mobility graphene, which is a significant improvement over previously strategized devices that are functional only for high mobility graphene [18–21,32].

B. Fabrication and experimental results

To experimentally verify the results, the cavity-coupled patterned graphene device was fabricated based on the schematic presented in Fig. 2(a) (see the method section for fabrication details). Large area CVD grown graphene was transferred on the substrate, and it was verified to be a monolayer by performing Raman characterization, as shown in Fig. 2(b). Figure 2(c) shows the scanning electron microscope (SEM) image of a nanoimprinted-patterned graphene showing good

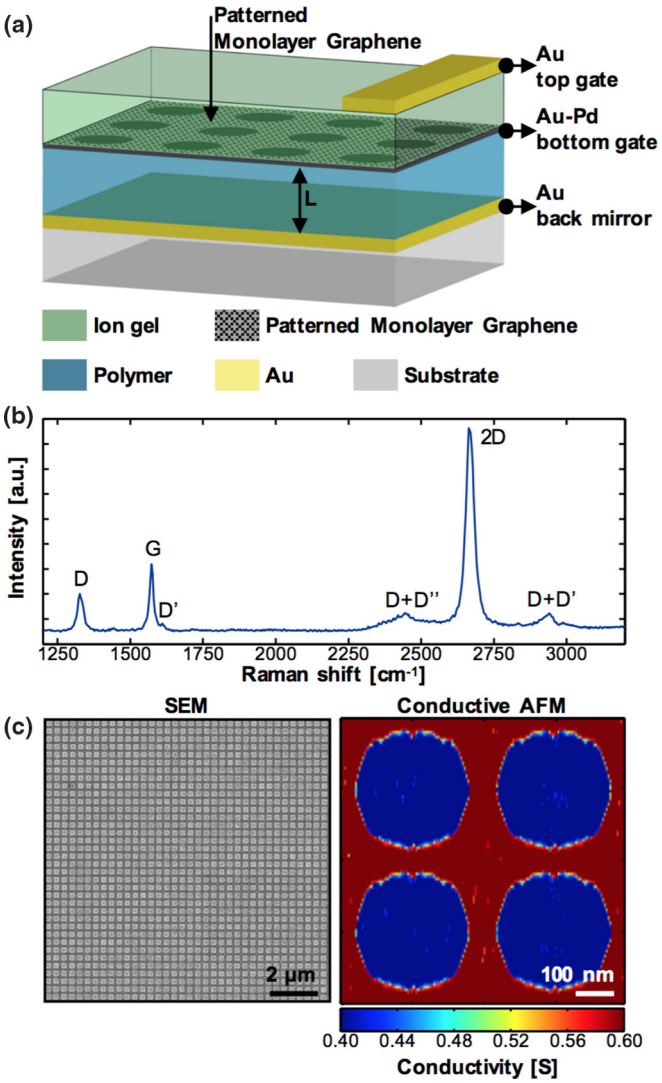

FIG. 2. Fabricated system and characterizations. (a) Schematic of the cavity-coupled patterned graphene. (b) Raman spectrum of grown pristine graphene. The presence of sharp and strong 2D peak proves monolayer graphene. (c) SEM image of the fabricated patterned graphene on dielectric slab (left) and Conductive AFM image of patterned graphene on copper foil (right).

uniformity in nanohole diameter across the patterned film. Furthermore, the graphene continuity and nanopattern formation was confirmed by conductive atomic force microscopy (AFM), which shows the difference in conductivity in the holes of the patterned graphene with respect to the surrounding [Fig. 2(d)].

We used ion gel as the dielectric layer to electrostatically dope patterned graphene. The measured capacitance of the ion gel layer is $C = 2.4\,\mu\text{F/cm}^2$ and its absorption in mid-IR spectrum is low. The Fermi energy of graphene is given by $E_F = \hbar v_F(\pi\rho)^{1/2}$, where $v_F \simeq 10^6$ m/s is the Fermi velocity and n is the electron/hole density obtained from $\rho = C\Delta V/e$, where ΔV is gate voltage relative to charge neutral point (CNP). The reported Fermi energies are calculated based on this relation. To estimate the corresponding Fermi energies experimentally, the conductivity of graphene sheet is calculated based on $\sigma(E_F) = \sigma_{\min}(1 + {E_F}^4/\Delta^4)^{1/2}$ [60], where $\sigma_{\min}$ is the minimum conductivity and Δ is the disorder strength parameter. As shown in Figs. S2a and S2b in the Supplemental Material [42], by fitting this conductivity to the experimental data (red dotted line), $\sigma_{\min} = 0.289$ ms/0.371 ms and $\Delta = 297$ meV/177 meV are obtained for the diagram shown in Figs. S2a/S2b, respectively. The relation between conductivity and mobility is $\sigma = \rho e \mu$, where μ is the carrier mobility of graphene. Fitting this equation (green solid line) to the experimental results yields $\mu = 250/960\,\text{cm}^2/\text{V s}$ for Figs. S2a/S2b. Positive and negative gate voltages correspond to n-doped and p-doped graphene, with a minimum conductivity occurring at the charge neutral point (CNP). According to this analysis we find that the CVD graphene sheet is p doped during growth and transfer ($\sim$0.05 eV).

For graphene absorption measurement, we followed a well-known technique to experimentally measure the reflection spectra of thin films and 2D materials [19–22,32–35,39,61,62]. In the experimental measurement with FTIR, we took the reflection spectrum of the structure shown in Fig. 4S in the Supplemental Material [42] (with unpatterned graphene) as the reference such that the FTIR calibrates the spectrum as $R = |r|^2 = 1$ in the entire wavelength range. Following this, the reflection spectrum (R) of the structure with patterned graphene is measured with respect to the reference. Due to the presence of the back mirror, the transmission (T) is zero and hence absorption (A) $= 1 - R - T = 1 - R$. This

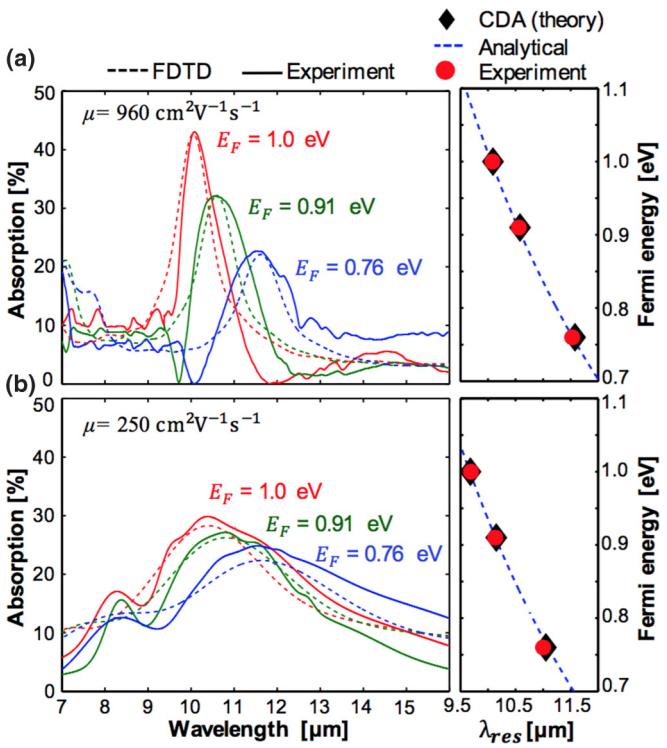

FIG. 3. Fabricated system and dynamic tunable response. Experimentally measured (solid) and theoretically predicted (dashed) mobility dependent tunable absorption spectra for a high (a) ($L = 1.1\,\mu$m) and low (b) ($L = 1.6\,\mu$m) mobility monolayer patterned graphene. Right figures showing the comparison of experimental, CDA, and theoretical results. Theoretical graphene plasmon frequency follows $\omega_p \propto \sqrt{E_F} \propto n^{1/4}$.

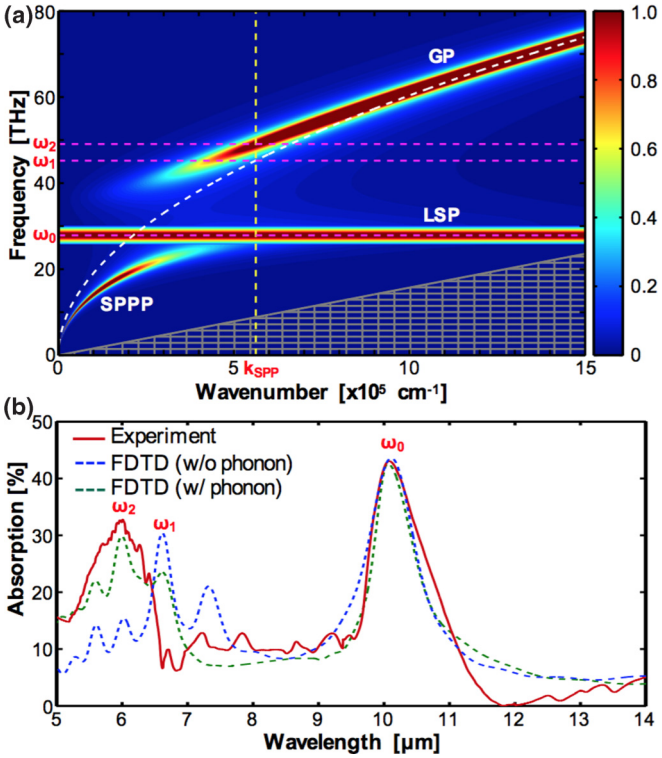

FIG. 4. Energy-loss dispersion. (a) Loss function for graphene with $E_F = 1.0$ eV. k_{spp} is the plasmon wave number associated with the second mode. ω_0, ω_1, and ω_2 represent the LSPR and the resonance propagating plasmon frequency without and with plasmon-phonon interaction, respectively. (b) Experimental and theoretical prediction of the plasmon excitation on patterned graphene with period = 400 nm, diameter = 330 nm, and $\mu = 960\,\mathrm{cm}^2/\mathrm{V\,s}$ coupled to an optical cavity with cavity thickness of 1.1 μm .

directly yields the absorption measurements shown in Figs. 3 and 4 which closely matches the FDTD predicted absorption spectra.

The simulated and measured absorption of the pristine graphene, patterned graphene, and cavity coupled-patterned graphene are shown in Figs. S3a and S3b, respectively. Figure 3 shows the FDTD simulated and experimentally measured electronically tunable absorption spectra of the cavity-coupled devices for high ($960\,\mathrm{cm}^2/\mathrm{V\,s}$) (a) and low ($250\,\mathrm{cm}^2/\mathrm{V\,s}$) (b) carrier mobility graphene. The carrier mobility is influenced by the degree of oxidation and polymer residues on the graphene surface. In both cases, E_F was varied between 0.7 and 1.0 eV. The high and low carrier mobility graphene devices exhibit a large ~2- and ~1-μm electrostatic tunability, respectively. The smaller peak in Fig. 3(b) left around 7.6 μm corresponds to polymer residue, which shows the effect of impurities in graphene's optical response. An increase in the Fermi energy leads to an increase in the electron density of graphene (ρ), which strengthens the electric dipole moment generated by the LSP resonance on the nanopatterned edges and therefore enhances light absorption, as shown in Fig. 3(b). As seen from Figs. 3(a) (right) and 3(b) (right), there is a good agreement between coupled dipole approximation (CDA) predictions, experimental measurements, and analytical graphene plasmon frequency $\omega_p \propto \sqrt{E_F} \propto \rho^{1/4}$ [63]. According to the experimental absorption spectra, the plasmon lifetimes ($\tau_{PL} = \hbar\Gamma^{-1}$) for high ($960\,\mathrm{cm}^2/\mathrm{V\,s}$) and low ($250\,\mathrm{cm}^2/\mathrm{V\,s}$) carrier mobility graphene are determined to be $\tau_{(\mathrm{PLhigh})} \approx 38$ fs and $\tau_{(\mathrm{PLlow})} \approx 16$ fs, respectively, which is compatible with the momentum relaxation time (τ).

C. Plasmon-phonon coupling

While the theoretical prediction using the FDTD method is in excellent agreement with the LSP peak locations (ω_0) in the experimental curves [Fig. 4(b)], it fails to explain the asymmetric line shape of the resonance. Hence, we can infer that in our device the effective combination of SU-8 polymer and the ion-gel matrix behaves as a polar substrate. Polar materials have ions of different valence, whose oscillating dipole moment gives rise to the interaction between electrons and optical phonons, called the Fröhlich interaction. The surface optical phonons in polar substrates are Fuchs-Kliewer-like [64]. By placing graphene on a polar substrate the long-range Fröhlich interaction mediates the interaction between optical phonons and surface plasmons in graphene [19]. The interaction between polar substrate/graphene phonons and electrons in graphene modifies substantially the graphene plasmon dispersion relation. The white dotted line in Fig. 4(a) represents the plasma frequency of graphene.

The dynamic polarizability

$$\boldsymbol{\chi}(\mathbf{q},\mathbf{i}\omega_{\mathbf{n}}) = -\frac{1}{A}\int_0^{\beta} \boldsymbol{d\tau}\, \boldsymbol{e}^{i\omega_n\tau}\, \langle \boldsymbol{T}\boldsymbol{\rho}_{\mathbf{q}}(\tau)\boldsymbol{\rho}_{-\mathbf{q}}(0)\rangle, \qquad (17)$$

determines several important quantities, such as effective electron-electron interaction, plasmon and phonon spectra, and Friedel oscillations. $\omega_n = \frac{2\pi n}{\beta}$ are Matsubara frequencies, $\boldsymbol{T}$ is time ordering operator, $\beta = 1/k_B T$, where k_B is the Boltzmann constant, and n is an integer number. ρ_q is the density operator in q space and A denotes the area of the sample. This quantity is calculated in the canonical ensemble for both of the sublattice density operators ($\rho = \rho_a + \rho_b$) [65]. The dynamic polarizability in the RPA regime is given by

$$\chi^{\mathrm{RPA}}(\mathbf{q},\omega) = \frac{\chi^0(\mathbf{q},\omega)}{\varepsilon^{\mathrm{RPA}}(\mathbf{q},\omega)}, \qquad (18)$$

where $\chi^0(\mathbf{q},\omega)$ is the noninteracting (zeroth order) polarizability (single pair bubble) and $\varepsilon^{\mathrm{RPA}}(\mathbf{q},\omega) = \varepsilon_m - v_c(\mathbf{q})\chi^0(\mathbf{q},\omega)$, with ε_m being the permittivity of the environment and $v_c(\mathbf{q}) = e^2/2\varepsilon_0 q$ the Coulomb interaction between the carriers. The RPA method corresponds to the expansion of $1/\varepsilon^{\mathrm{RPA}}(\mathbf{q},\omega)$, leading to an infinite power series over the bubble diagrams. If optical phonons are also considered, the effective dielectric function in the RPA expansion takes the form [19,66]

$$\begin{aligned}\varepsilon^{\mathrm{RPA}}(\mathbf{q},\omega) = \varepsilon_m &- v_c(\mathbf{q})\chi^0(\mathbf{q},\omega) \\ &- \varepsilon_m \sum_l v_{\mathrm{sph},l}(\mathbf{q},\omega)\chi^0(\mathbf{q},\omega) \\ &- \varepsilon_m v_{\mathrm{oph}}(\mathbf{q},\omega)\chi^0_{j,j}(\mathbf{q},\omega). \end{aligned} \qquad (19)$$

The third term is the effective dielectric function for different phonon modes (l) coming from the electron-electron interaction mediated by substrate optical phonons, which

couple to the electrons by means of the Fröhlich interaction, $v_{\mathrm{sph},l}(\mathbf{q},\omega) = |M_{\mathrm{sph}}|^2 G_l^0(\omega)$, where $|M_{\mathrm{sph}}|^2$ is the scattering and G_l^0 is the free phonon Green's function. The last term of Eq. (19) corresponds to graphene's optical-phonon mediated electron-electron interaction, $v_{\mathrm{oph}}(\mathbf{q},\omega) = |M_{\mathrm{oph}}|^2 G^0(\omega)$. Here $|M_{\mathrm{oph}}|^2$ defines the scattering matrix element and $G^o(\omega)$ is the free phonon Green's function. In Eq. (19), $\chi^0_{j,j}(\mathbf{q},\omega)$ is the current-current correlation function. By taking the decay rate $\omega \to \omega + i\tau^{-1}$ into account, the dynamic polarizability reduces to $\chi^0(\mathbf{q},\omega) \approx E_F q^2/\pi\hbar^2(\omega + i\tau^{-1})^2$ [19,65]. The momentum relaxation time (τ) can be derived by considering the impurity, electron-phonon interaction and the scattering related to nanostructure edges $\tau = {\tau_{\mathrm{DC}}}^{-1} + {\tau_{\mathrm{edge}}}^{-1} + {\tau_{e-\mathrm{ph}}}^{-1}$ [19,54], which determines the plasmon lifetime and the absorption spectrum bandwidth. It can be evaluated via the measured dc mobility μ of the graphene sample using $\tau_{\mathrm{DC}} = \mu\hbar\sqrt{\pi\rho}/ev_F$, where $v_F \sim 10^6$m/s is the Fermi velocity and $\rho = (E_F/\hbar v_F)^2/\pi$ is the charge-carrier density. $\tau_{\mathrm{edge}} \approx (1 \times 10^6/w - w_0)^{-1}$ is due to the scattering from the nanostructure edges, where w is the edge-to-edge distance of the holes, $w_0 \approx 7$ nm is the parameter that includes edge effects, and $\tau_{e-\mathrm{ph}} = \hbar/2\mathrm{Im}(\sum_{e-\mathrm{ph}})$ is related to the scattering because of electron-phonon coupling. $\mathrm{Im}(\sum_{e-\mathrm{ph}}) = \gamma|\hbar\omega - \mathrm{sgn}(\hbar\omega - E_F)\hbar\omega_{\mathrm{oph}}|$, where $\sum_{e-\mathrm{ph}}$ is the electron self-energy, $\gamma = 18.3 \times 10^{-3}$ is a dimensionless constant describing the electron-phonon coupling coefficient, and $\hbar\omega_{\mathrm{oph}} \approx 0.2$ eV is the graphene optical-phonon energy [54]. From this it is evident that the plasmon lifetime is reduced due to the electron-phonon interaction and edge scattering, but the dc conductivity which is used to calculate the dielectric function of graphene is invariant if the edge-to-edge distance of the pattern is more than the carrier mean free path ($L_{\mathrm{MFP}} = v_F\tau_{\mathrm{DC}}$). The modified Drude model is not valid for a patterned graphene sheet only if the edge-to-edge distance is much smaller than the carrier mean free path of electrons and holes. For the chosen pattern and carrier mobility ($\mu = 960\,\mathrm{cm}^2/\mathrm{V\,s}$), the carrier mean free path ($L_{\mathrm{MFP}} = v_F\tau_{\mathrm{dc}} < 42$ nm) is smaller than the edge-to-edge distance (=70 nm), which means that the modified Drude model is a good approximation for the dielectric function of this patterned graphene sheet. In presence of hard boundaries, atomic displacement vanishes at the boundaries, thereby modifying the acoustic and optical-phonon dispersion. This means we need to consider a graphene nanoribbon (GNR) with zigzag-edge or armchair-edge and N periods (N is the number atoms between two edges) with several quantized vibration modes. This model is applied in the long-wavelength limit, therefore only the lowest vibration modes up to $N/2$ appear. By applying the boundary conditions to the displacement equation, the longitudinal (LO) and transverse (TO) optical-phonon branches are changed, i.e., $\omega_n^2 = \omega_{\mathrm{LO}}^2 - \lambda^2(q_n^2 + q^2)^2 + \beta_L^2(q_n^2 + q^2)$ and $\omega_n^2 = \omega_{\mathrm{TO}}^2 - \beta_T^2(q_n^2 + q^2)$. This means the optical-phonon frequency, which is almost the same for both branches (LO and TO), shifts from $\omega_{\mathrm{op}} \sim 1581\,\mathrm{cm}^{-1}$ to $\omega_{\mathrm{op}} \sim 1591\,\mathrm{cm}^{-1}$ for both zigzag-edge and armchair-edge GNR [67–69]. We used this modified optical-phonon frequency in Fig. 4. The effect of this change is very small.

The coupling of plasmon and substrate/graphene phonon can be characterized through the loss function (Z), which is the imaginary part of inverse effective dielectric function calculated via the generalized RPA theory [18,19],

$$Z \propto -\mathrm{Im}\left(\frac{1}{\varepsilon^{\mathrm{RPA}}}\right). \tag{20}$$

The loss function represents the amount of energy dissipated by exciting the plasmon coupled to the substrate and optical phonons in graphene. The surface plasmons in graphene are damped through radiative and nonradiative processes [70]. Nonradiative damping transfers the plasmon energy to hot electron-hole excitation by means of intraband transition. Figure 4(a) shows the loss function for graphene with carrier mobility $\mu = 960\,\mathrm{cm}^2/\mathrm{V\,s}$ and $E_F = 1.0$ eV. The thickness of the optical cavity is chosen to be 1.1 μm such that the first (ω_0) and second (ω_2) modes lead to 44% and 33% light absorption, respectively. The plasmon assisted electron-hole pair generation in this structure lies outside the Landau intraband damping region, indicated by the shaded area in Fig. 4(a). A band gap in the plasmon-phonon dispersion relation is formed via Fröhlich interaction between graphene plasmons and optical phonons [71]. This coupling leads to the splitting of the energy into two distinct branches: surface plasmon phonon polaritons (SPPPs) and graphene plasmons (GPs) [19,21,65,66,71]. The horizontal branch line marked as ω_0 is the LSP mode in Fig. 1(a) and is independent of the plasmon wave vector due to the localization of the LSP. The asymmetric line shape of the first band (ω_0) in Fig. 4(b), which is observed in experiments, is due to the merging of these two bands (LSP and SPPP). Figure 4(a) shows a clear blueshift in the GP band at a wave vector ($k_{\mathrm{sp}} \approx 5.5 \times 10^5\mathrm{cm}^{-1}$), corresponding to the edge-to-edge distance between the holes in the presence of edge effect. Interestingly, there exists a discrepancy in the location of the second mode peak of the FDTD curve simulated without accounting for optical phonons (ω_1) from that of the experimental spectrum (ω_2) [Fig. 4(b)]. This is attributed to the plasmon-phonon coupling, and we show that by inserting the plasmon-phonon interaction as a perturbation and using $\varepsilon^{\mathrm{RPA}}(\mathbf{q},\omega)$ in Eq. (19) as effective graphene dielectric function in the FDTD simulations, one can recover the experimentally observed blueshift, as illustrated in Fig. 4(b) by the green dotted line. The simple Drude model cannot capture the plasmon-phonon interactions which leads to discrepancies between FDTD predictions and experimental measurements as can be observed in Fig. 4(b). In the long-wavelength regime, by substituting $\chi^0(\mathbf{q},\omega) \approx E_F q^2/\pi\hbar^2(\omega + i\tau^{-1})^2$ and v_c into Eq. (19), the second term on the right-hand side is reduced to the Drude model dielectric function

$$\varepsilon_{\mathrm{Drude}} = -v_c(\mathbf{q})\chi^0(\mathbf{q},\omega) = -\frac{e^2 E_f q}{2\varepsilon_0\pi\hbar^2(\omega + i\tau^{-1})^2}. \tag{21}$$

According to Eq. (21), the in-plane momentum of the pristine graphene should be equal to $q = \frac{2}{t}$. In Eq. (19), the phonon terms, which are small relative to $\varepsilon^{\mathrm{Drude}}$, perturb the original system. In order to include the electron-phonon coupling in the simulation and to predict the experimental results with higher accuracy, Eq. (19) has been used as the input data in the FDTD simulations to generate the plasmon-phonon dispersion diagram of Fig. 4(b) with much improved correspondence between prediction and experimental observation.

This analysis explains different processes involved in the experimental results and the physical optoelectronic phenomena and highlights the plasmon-phonon interaction leads to the hybridization of the plasmon dispersion relation, which gives rise to a blueshift in the propagating surface plasmon spectrum. However, the main absorption peak (ω_0), which originates from LSP, remains unperturbed due to frequency domain separation between the phonon and LSP resonances.

III. CONCLUSION

In conclusion, we have presented a scheme to increase the light-graphene interaction by the direct excitation of plasmons on patterned monolayer graphene coupled to an optical cavity. Our design of a square lattice of holes on graphene, which is experimentally realized following a simple nanoimprinting technique, not only preserves material continuity for electronic conductivity, which is essential for optoelectronic devices, but also leads to direct plasmon excitation that is independent of the incident light polarization. Therefore, our design outperforms other nanoribbon based devices whose absorption is polarization dependent, thereby reducing their performance for unpolarized light. This approach triggers the direct excitation of cavity-coupled plasmon in CVD grown monolayer graphene with a cavity thickness of $L = 1.1\,\mu$m and yields an experimentally observed absorption of ∼45%, which is the highest value reported so far in the 8–12-μm band. We show that a reduction in carrier mobility of graphene decreases the absorption to ∼30%, which is nonetheless higher than previous studies. Furthermore, electronically controlled dynamic tunability (∼2 μm) is successfully demonstrated. We have shown experimentally and theoretically that the carrier mobility of graphene, which is influenced by the defect density, determines the enhanced absorption bandwidth and line shape. Further, CVD grown graphene quality, pattern, gating optimizations, and alternative low-absorbance dielectrics as gating materials are needed in order to reach the theoretical maximum absorption of ∼60% for a cavity thickness of $L = 1.6\,\mu$m. Such voltage tunable high absorption in monolayer graphene will enable the development of various practical graphene based optoelectronic devices like photodetectors, sensors, modulators, etc.

ACKNOWLEDGMENTS

This work at University of Central Florida was supported by DARPA under the WIRED program Grant No. HR0011-16-1-0003 and by NSF Grant No. CCF-1514089.

D.C. conceived the idea. A.S. designed and performed the experiments. J.C., D.F., A.V.G., and S.C. provided technical assistance. A.S., M.L., and D.C. analyzed and simulated the data. J.C., L.T., L.Z., M.L., and D.C. contributed materials/analysis tools. A.S., S.C., M.L., and D.C. co-wrote the paper. The authors declare no competing financial interests.

APPENDIX: METHODS

1. Device fabrication process

The graphene sheet is grown on a 25–μm-thick copper foil in an oven composed of a molten silica tube heated in a split tube furnace. The molten silica tube and copper foil are loaded inside the furnace, evacuated, back filled with hydrogen, and heated up to 1000 °C while keeping a 50-SCCM (Standard Cubic Centimeters per Minute) H_2 stream. The subsequent steps include reinstating the copper foil at 1000 °C for 30 min, inserting 80 SCCM of CH_4 for 30 min. Then the furnace is cooled down to room temperature without gas feeding. An optically thick layer of Cr/Au (4 nm / 200 nm) is deposited on a glass substrate as a back reflector using *e*-beam deposition. A photoresist (SU-8) layer is spin-coated on the gold back reflector to form an optical cavity, that is cured under UV lamp for 2 h and baked on a hot plate for 1 h at 95 °C in order to complete the cross-linking process. A thin layer (∼20 nm) of gold-palladium (Au-Pd) is sputtered on the dielectric spacer which function as a gate electrode. A CVD-grown graphene sheet is transferred onto the Au-Pd layer using a PMMA transfer layer which is subsequently dissolved in acetone. The square lattice hole pattern is fabricated following a simple large area nanoimprinting technique [35,39]. A poly dimethylsiloxane (PDMS) stamp is embossed against a thin photoresist (SU-8) layer that is spun coated on the graphene layer, followed by reactive ion etcher (RIE) in order to perforate the graphene layer. Low carrier mobility nanomesh graphene is prepared by rinsing the residual polymers (PMMA and SU-8) in acetone one time for a few seconds. In contrast, the high carrier mobility sample is prepared by repeating this process for more than ten times in order to reduce plolymer residues from the perforated graphene. A high capacitance ion gel film with refractive index of 1.3 [72] is drop-casted on graphene in order to tune its Fermi energy to high values (∼1 eV). Ion gel is a printable gate dielectric polymer [32,73] made by mixing ionic liquid ([EMIM][TFSI]) (Sigma-Aldrich, Inc.) with dry PS-PEO-PS (10-44-10 kg/mol) triblock copolymer (Polymer Source, Inc.) with ratio 1:0.04 in a dry solvent (dichloromethane) (Sigma-Aldrich, Inc.) and by stirring the mixture overnight. Then it is left for 48 h inside a high vacuum chamber (pressure $< 10^{-6}$ torr) in order to evaporate the remaining solvent. The materials are dried in high vacuum for 24 h then transferred to the glovebox for 4 days. The gate is fabricated by depositing Cr/Au (3 nm / 40 nm) on Si substrate. A copper wire is connected to the gate by applying silver paste on the side and back. The resulting substrate is flipped upside down and put on top of the ion gel.

2. Materials characterization and measurement

After RIE and the polymer removal, conductive AFM was used to confirm the presence of a patterned graphene layer on the substrate. After patterning the graphene on copper foil following the same procedure and parameters used to pattern the graphene sheet on the SU-8 layer, conductive AFM (MultiMode, Atomic Force Microscope, Nanoscope III, Digital Instruments, Santa Barbara, California) is employed to map of conductivity of the patterned graphene with nanoscale spatial resolution. Conductive (Au coated) cantilevers with spring constant $k = 0.06\,\mathrm{N/m}$ was used. Measurements are performed in contact mode and a full IV curve was collected at each pixel of the image. The theoretical simulations are done by finite-difference time-domain (FDTD) method using

Lumerical FDTD (Lumerical Inc.) software. The Raman spectrum of the grown graphene sheet is measured by WITec Renishaw RM 1000B Micro-Raman Spectrometer with an excitation laser wavelength of 514 nm and a 50x objective lens. The real and imaginary parts of the gold dielectric function used in simulations are taken from Palik [74]. The corresponding optical absorption measurements are performed with a microscope-coupled FTIR (Bruker Inc., Hyperion 1000-Vertex 80). The mobility is measured by using the model 2450 SourceMeter® SMU instrument and a four-point probe. We applied the gate voltage between bottom and top gate with ion gel as dielectric in presence of "patterned graphene" with two probes and measured the electrical conductivity through source-drain using other probes.

[1] F. Bonaccorso, Z. Sun, T. Hasan, and A. C. Ferrari, Nat. Photon. **4**, 611 (2010).

[2] L. A. Falkovsky, J. Exp. Theor. Phys. **106**, 575 (2008).

[3] L. A. Falkovsky and S. S. Pershoguba, Phys. Rev. B **76**, 153410 (2007).

[4] L. A. Falkovsky and A. A. Varlamov, Eur. Phys. J. B **56**, 281 (2007).

[5] V. Singh, D. Joung, L. Zhai, S. Das, S. I. Khondaker, and S. Seal, Prog. Mater. Sci. **56**, 1178 (2011).

[6] F. Schwierz, Nat. Nanotechnol. **5**, 487 (2010).

[7] X. Gan, R. J. Shiue, Y. Gao, K. F. Mak, X. Yao, L. Li, A. Szep, D. Walker, Jr., J. Hone, T. F. Heinz, and D. Englund, Nano Lett. **13**, 691 (2013).

[8] Y. Yao, R. Shankar, M. A. Kats, Y. Song, J. Kong, M. Loncar, and F. Capasso, Nano Lett. **14**, 6526 (2014).

[9] M. Liu, X. Yin, E. Ulin-Avila, B. Geng, T. Zentgraf, L. Ju, F. Wang, and X. Zhang, Nature (London) **474**, 64 (2011).

[10] Z. Sun and H. Chang, ACS Nano **8**, 4133 (2014).

[11] M. Freitag, T. Low, W. Zhu, H. Yan, F. Xia, and P. Avouris, Nat. Commun. **4**, 1951 (2013).

[12] Z. Liu, S. P. Lau, and F. Yan, Chem. Soc. Rev. **44**, 5638 (2015).

[13] Z. Sun, T. Hasan, F. Torrisi, D. Popa, G. Privitera, F. Wang, F. Bonaccorso, D. M. Basko, and A. C. Ferrari, ACS Nano **4**, 803 (2010).

[14] R. R. Nair, P. Blake, A. N. Grigorenko, K. S. Novoselov, T. J. Booth, T. Stauber, N. M. Peres, and A. K. Geim, Science **320**, 1308 (2008).

[15] H. Yan, F. Xia, W. Zhu, M. Freitag, C. Dimitrakopoulos, A. A. Bol, G. Tulevski, and P. Avouris, ACS Nano **5**, 9854 (2011).

[16] A. R. Banman and J. Heyman, Macalester J. Phys. Astron. **3**, 2 (2015).

[17] H. P. Paudel, A. Safaei, and M. N. Leuenberger, in *Nanoplasmonics in Metallic Nanostructures and Dirac Systems*, edited by G. Barbillon (Intech, Croatia, 2017), Chap. 3.

[18] L. Ju, B. Geng, J. Horng, C. Girit, M. Martin, Z. Hao, H. A. Bechtel, X. Liang, A. Zettl, Y. R. Shen, and F. Wang, Nat. Nanotechnol. **6**, 630 (2011).

[19] H. G. Yan, T. Low, W. J. Zhu, Y. Q. Wu, M. Freitag, X. S. Li, F. Guinea, P. Avouris, and F. N. Xia, Nat. Photon. **7**, 394 (2013).

[20] Z. Fang, S. Thongrattanasiri, A. Schlather, Z. Liu, L. Ma, Y. Wang, P. M. Ajayan, P. Nordlander, N. J. Halas, and F. J. Garcia de Abajo, ACS Nano **7**, 2388 (2013).

[21] V. W. Brar, M. S. Jang, M. Sherrott, J. J. Lopez, and H. A. Atwater, Nano Lett. **13**, 2541 (2013).

[22] M. S. Jang, V. W. Brar, M. C. Sherrott, J. J. Lopez, L. Kim, S. Kim, M. Choi, and H. A. Atwater, Phys. Rev. B **90**, 165409 (2014).

[23] M. Grande, M. A. Vincenti, T. Stomeo, G. V. Bianco, D. de Ceglia, N. Akozbek, V. Petruzzelli, G. Bruno, M. De Vittorio, M. Scalora, and A. D'Orazio, Opt. Express **22**, 31511 (2014).

[24] N. K. Emani, T. F. Chung, X. Ni, A. V. Kildishev, Y. P. Chen, and A. Boltasseva, Nano Lett. **12**, 5202 (2012).

[25] M. Furchi, A. Urich, A. Pospischil, G. Lilley, K. Unterrainer, H. Detz, P. Klang, A. M. Andrews, W. Schrenk, G. Strasser, and T. Mueller, Nano Lett. **12**, 2773 (2012).

[26] T. Otsuji, V. Popov, and V. Ryzhii, J. Phys. D.: Appl. Phys. **47**, 094006 (2014).

[27] Y. Zhang, Y. Feng, B. Zhu, J. Zhao, and T. Jiang, Opt. Express **22**, 22743 (2014).

[28] A. Majumdar, J. Kim, J. Vuckovic, and F. Wang, IEEE J. Sel. Top. Quantum Electron. **20**, 4600204 (2014).

[29] A. M. Brown, R. Sundararaman, P. Narang, W. A. Goddard, III, and H. A. Atwater, ACS Nano **10**, 957 (2016).

[30] R. Alaee, M. Farhat, C. Rockstuhl, and F. Lederer, Opt. Express **20**, 28017 (2012).

[31] S. Thongrattanasiri and F. J. Garcia de Abajo, Phys. Rev. Lett. **110**, 187401 (2013).

[32] Z. Fang, Y. Wang, A. E. Schlather, Z. Liu, P. M. Ajayan, F. J. de Abajo, P. Nordlander, X. Zhu, and N. J. Halas, Nano Lett. **14**, 299 (2014).

[33] D. Franklin, Y. Chen, A. Vazquez-Guardado, S. Modak, J. Boroumand, D. Xu, S. T. Wu, and D. Chanda, Nat. Commun. **6**, 7337 (2015).

[34] A. Vazquez-Guardado, A. Safaei, S. Modak, D. Franklin, and D. Chanda, Phys. Rev. Lett. **113**, 263902 (2014).

[35] D. Chanda, K. Shigeta, T. Truong, E. Lui, A. Mihi, M. Schulmerich, P. V. Braun, R. Bhargava, and J. A. Rogers, Nat. Commun. **2**, 479 (2011).

[36] A. Y. Nikitin, P. Alonso-Gonzalez, S. Velez, S. Mastel, A. Centeno, A. Pesquera, A. Zurutuza, F. Casanova, L. E. Hueso, F. H. L. Koppens, and R. Hillenbrand, Nat. Photon. **10**, 239 (2016).

[37] Z. Fei, M. D. Goldflam, J. S. Wu, S. Dai, M. Wagner, A. S. McLeod, M. K. Liu, K. W. Post, S. Zhu, G. C. Janssen, M. M. Fogler, and D. N. Basov, Nano Lett. **15**, 8271 (2015).

[38] A. Yu. Nikitin, F. Guinea, F. J. García-Vidal, and L. Martín-Moreno, Phys. Rev. B **84**, 161407(R) (2011).

[39] D. Chanda, K. Shigeta, S. Gupta, T. Cain, A. Carlson, A. Mihi, A. J. Baca, G. R. Bogart, P. Braun, and J. A. Rogers, Nat. Nanotechnol. **6**, 402 (2011).

[40] W. S. Weiglhofer, A. Lakhtakia, and B. Michel, Microwave Opt. Technol. Lett. **22**, 221 (1999).

[41] C. G. Granqvist and O. Hunderi, Phys. Rev. B **18**, 1554 (1978).

[42] See Supplemental Material at http://link.aps.org/supplemental/10.1103/PhysRevB.96.165431 for four figures related to the simulation convergence for different shutoff minimum values,

carrier mobility measurement results, simulated and experimental absorption spectra of the optical graphene without graphene, with pristine graphene and patterned graphene and moreover the schematic of the structure with unpatterned and patterned graphene.

[43] S. Thongrattanasiri, F. H. Koppens, and F. J. Garcia de Abajo, Phys. Rev. Lett. **108**, 047401 (2012).

[44] S. A. Maier, *Plasmonic: Fundamentals and Applications* (Springer, New York, 2007).

[45] F. H. Koppens, D. E. Chang, and F. J. Garcia de Abajo, Nano Lett. **11**, 3370 (2011).

[46] W. Gao, J. Shu, C. Qiu, and Q. Xu, ACS Nano **6**, 7806 (2012).

[47] G. W. Hanson, J. Appl. Phys. **103**, 064302 (2008).

[48] A. Y. Nikitin, F. Guinea, and L. Martin-Moreno, Appl. Phys. Lett. **101**, 151119 (2012).

[49] A. Y. Nikitin, F. Guinea, F. J. Garcia-Vidal, and L. Martin-Moreno, Phys. Rev. B **85**, 081405(R) (2012).

[50] D. V. van Coevorden, R. Sprik, A. Tip, and A. Lagendijk, Phys. Rev. Lett. **77**, 2412 (1996).

[51] L. L. Zhao, K. L. Kelly, and G. C. Schatz, J. Phys. Chem. B **107**, 7343 (2003).

[52] H. Hirai, H. Tsuchiya, Y. Kamakura, N. Mori, and M. Ogawa, J. Appl. Phys. **116**, 083703 (2014).

[53] Z. Fei, A. S. Rodin, G. O. Andreev, W. Bao, A. S. McLeod, M. Wagner, L. M. Zhang, Z. Zhao, M. Thiemens, G. Dominguez, M. M. Fogler, A. H. Castro Neto, C. N. Lau, F. Keilmann, and D. N. Basov, Nature (London) **487**, 82 (2012).

[54] M. Jablan, H. Buljan, and M. Soljacic, Phys. Rev. B **80**, 245435 (2009).

[55] H. S. Song, S. L. Li, H. Miyazaki, S. Sato, K. Hayashi, A. Yamada, N. Yokoyama, and K. Tsukagoshi, Sci. Rep. **2**, 337 (2012).

[56] J. H. Chen, W. G. Cullen, C. Jang, M. S. Fuhrer, and E. D. Williams, Phys. Rev. Lett. **102**, 236805 (2009).

[57] C. R. Dean, A. F. Young, I. Meric, C. Lee, L. Wang, S. Sorgenfrei, K. Watanabe, T. Taniguchi, P. Kim, K. L. Shepard, and J. Hone, Nat. Nanotechnol. **5**, 722 (2010).

[58] J. D. Jackson, *Classical Electrodynamics*, 3th ed. (Wiley, New York, 1998).

[59] N. W. Ashcroft and N. D. Mermin, *Solid State Physics* (Rinehart and Winston, New York, 1978).

[60] J. C. Song, M. S. Rudner, C. M. Marcus, and L. S. Levitov, Nano Lett. **11**, 4688 (2011).

[61] J. S. Ponraj, Z. Q. Xu, S. C. Dhanabalan, H. Mu, Y. Wang, J. Yuan, P. Li, S. Thakur, M. Ashrafi, K. McCoubrey, Y. Zhang, S. Li, H. Zhang, and Q. Bao, Nanotechnology **27**, 462001 (2016).

[62] Y. Liu, A. Chadha, D. Zhao, J. R. Piper, Y. Jia, Y. Shuai, L. Menon, H. Yang, Z. Ma, S. Fan, F. Xia, and W. Zhou, Appl. Phys. Lett. **105**, 181105 (2014).

[63] E. H. Hwang and S. Das Sarma, Phys. Rev. B **75**, 205418 (2007).

[64] R. Fuchs and K. L. Kliewer, Phys. Rev. **140**, A2076 (1965).

[65] B. Wunsch, T. Stauber, F. Sols, and F. Guinea, New J. Phys. **8**, 318 (2006).

[66] E. H. Hwang, R. Sensarma, and S. Das Sarma, Phys. Rev. B **82**, 195406 (2010).

[67] J. Qian, M. J. Allen, Y. Yang, M. Dutta, and M. A. Stroscio, Superlattices Microstruct. **46**, 881 (2009).

[68] A. A. Balandin, Nat. Mater. **10**, 569 (2011).

[69] D. L. Nika and A. A. Balandin, J. Phys.: Condens. Matter **24**, 233203 (2012).

[70] R. Sundararaman, P. Narang, A. S. Jermyn, W. A. Goddard, III, and H. A. Atwater, Nat. Commun. **5**, 5788 (2014).

[71] R. Jalabert and S. Das Sarma, Phys. Rev. B **40**, 9723 (1989).

[72] H. Weingartner, P. Sasisanker, C. Daguenet, P. J. Dyson, I. Krossing, J. M. Slattery, and T. Schubert, J. Phys. Chem. B **111**, 4775 (2007).

[73] J. H. Cho, J. Lee, Y. Xia, B. Kim, Y. He, M. J. Renn, T. P. Lodge, and C. D. Frisbie, Nat. Mater. **7**, 900 (2008).

[74] E. D. Palik, J. Opt. Soc. Am. A **1**, 1297 (1984).